Neural Network Sampling of the Free Energy Landscape for Nitrogen Dissociation on Ruthenium

Elizabeth M. Y. Lee,[1,‡] Thomas Ludwig,[2,3,‡] Boyuan Yu,[1] Aayush R. Singh,[2,†]

François Gygi,[4] Jens K. Nørskov,[2,3,5] and Juan J. de Pablo[1,6]**

[1]Pritzker School of Molecular Engineering, The University of Chicago, Chicago, Illinois 60637, USA

[2]SUNCAT Center for Interface Science and Catalysis, Department of Chemical Engineering, Stanford University, Stanford, California 94305, United States

[3]SUNCAT Center for Interface Science and Catalysis, SLAC National Accelerator Laboratory, 2575 Sand Hill Road, Menlo Park, California 94025, United States

[4]Department of Computer Science, University of California, Davis, California 95616, USA

[5]Department of Physics, Technical University of Denmark, Lyngby 2800, Denmark

[6]Argonne National Laboratory, 9700 Cass Avenue, Lemont, IL 60439, USA.

[‡]These authors contributed equally

Corresponding Author

*Emails: jkno@dtu.dk (J.K.N.); depablo@uchicago.edu (J.J.d.P.)

ABSTRACT: Reaction rates in heterogeneous catalysis are predicted using the free energy profiles of elementary reactions. Conventionally, the energetics are computed from critical points of the potential energy surface, with harmonic free energy corrections. Here we use *ab initio* molecular dynamics and neural network-assisted enhanced sampling simulations to directly calculate the free energy landscape of a prototypical heterogeneous catalysis reaction, the dissociation of molecular nitrogen on ruthenium. We show that accelerating force- and frequency-based enhanced sampling using neural networks can characterize reactive phenomena at density functional theory-level accuracy. A previously reported molecularly adsorbed metastable state is found in the potential energy surface but is absent in the free energy surface. The potential of mean force for the dissociation reaction shows significant temperature-dependent effects beyond the standard harmonic approximation. We demonstrate that these thermodynamic effects can be important for elementary reactions on transition metal surfaces.

TOC GRAPHIC:

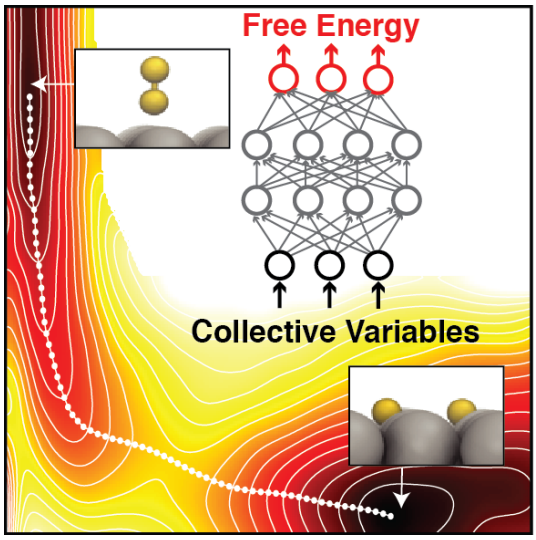

KEYWORDS: heterogeneous catalysis, chemical reactions, free energy, *ab initio* molecular dynamics, enhanced sampling, artificial neural networks

Reactions of molecules on solid surfaces are the basis for many industrial chemical processes, including semiconductor processing, corrosion, electrochemistry, and heterogeneous catalysis.[1–3] A prototypical reaction for understanding key concepts in heterogeneous catalysis is the catalytic synthesis of ammonia, a large-scale industrial reaction worldwide.[4,5] On ruthenium, one of the most active catalysts for ammonia synthesis, the rate-determining step is the dissociation of molecular nitrogen.[6] There have been numerous experimental and theoretical studies on the energetics of this process. Surface science techniques such as reactive scattering, molecular beam, and laser-assisted associated desorption have measured dissociation probabilities and energy barriers of N_2 on Ru(0001).[7–15] For these surface catalytic reactions, density functional theory (DFT) is widely used to predict reaction energies and activation barriers.[2,14,16–23]

Early DFT studies of N_2 on Ru(0001) have computed dissociation free energy barriers on the basis of normal mode analysis with the harmonic approximation (HA) and showed reasonable agreement with thermal rate experiments.[6] These calculations require the predetermination of local minima and transition states of the potential energy surface (PES) and do not capture anharmonic contributions. A standard practice within surface science is to use a single, lowest-energy configuration for each intermediate state and the normal modes of only the adsorbate atoms to predict free energies. However, recent theoretical and experimental investigations of larger reacting molecules or structurally complex catalytic materials, like metal organic frameworks (MOFs), have reported appreciable entropic contributions to the reaction barriers and rates beyond standard HA, such as configurational multiplicity and anharmonicity.[24–28] These findings suggest that extending free energy calculations beyond the conventional harmonic approach is essential for predicting free energy barriers and determining the reactive configurations.

While the free energies of surface reactions at finite temperature and pressure can in principle be directly calculated from dynamical simulations using DFT, *i.e.*, *ab initio* molecular dynamics (AIMD), these simulations are computationally demanding (*e.g.*, several hundred electrons) and limited to short-time scales (*e.g.*, tens to hundreds of picoseconds). Recent works on N_2 on Ru and other molecule-surface reactions have circumvented this problem by replacing DFT with neural network-based potentials[18,19,29] or empirical interatomic potentials[30–32]. Here we develop and apply an enhanced sampling approach to map the free energy landscape of N_2 undergoing molecular dissociation on Ru using AIMD, where forces and energies are computed directly from DFT.

Enhanced sampling methods enable the efficient calculation of the potential of mean force (PMF) or the free energy surface (FES) along the reaction coordinate by accelerating dynamic simulations. Adaptive enhanced sampling methods, such as metadynamics and adaptive biasing force (ABF), explore the configurational space by adding an adaptively computed bias to the original dynamics. Until recently[26,33–42], these approaches focused on classical systems[43–45] with few surface chemistry applications. In the last two years, machine learning-assisted enhanced sampling methods have been introduced to accelerate sampling efficiency over existing methods.[46–51] The combined-force frequency (CFF) approach[47] uses Bayesian regularized artificial neural networks (BRANN) to represent the bias based on the PMF and its gradient, combining several concepts from existing methods, such as metadynamics and ABF. However, the generalizability of these emerging methodologies to reactive systems on materials modeled with electronic structure calculations has not yet been demonstrated.

In this work, we present a DFT description of the PMF for dissociation of N_2 on Ru(0001) using a neural network-based enhanced sampling method called CFF with AIMD (i.e., CFF-

AIMD). We show that neural networks accelerate enhanced sampling simulations to predict the long-timescale surface reaction phenomenon using AIMD. We find that the entropies of the intermediate states affect the topology of the FES, which consequently deviates from the PES. We use several variants of HA to show that the computed PMF using CFF-AIMD captures temperature-dependent contributions to the free energies that are not included in conventional HA methods, such as the effects of multiple dissociated states, configurational degeneracies, and vibrational entropy of surface atoms. We demonstrate that these entropic effects can be critical for predicting the energetics of elementary reactions on metal surfaces.

Free energy calculations with enhanced sampling simulations are less computationally demanding using unbiased AIMD but can require a large number of DFT calculations to converge sampling statistics and quantify statistical uncertainties. Therefore, we adopt a computationally efficient DFT model, consisting of a 2×2 unit cell of an N_2 molecule on a two-layer Ru(0001) surface (Figure 1A) (see Computational Methods). In CFF-AIMD simulations, we use two-dimensional (2D) collective variables (CVs) to describe the bond breaking/formation and adsorption/desorption processes for the dissociation of N_2 on Ru: the N-N distance (r) and the molecule-surface distance (Z) (Figure 1A). An ensemble of final dissociated states (2N*) can be sampled because there are two stable N* adsorption sites: hexagonal close-packed (HCP) hollow and face-centered cubic (FCC) hollow sites, which differ in the presence of a ruthenium atom in the layer below the HCP hollow site (Figure 1B). In total, we performed ~500 ps of enhanced sampling simulations using multiple walkers, amounting to ~17 million timesteps (see Table S2 for a summary of simulations performed in this work).

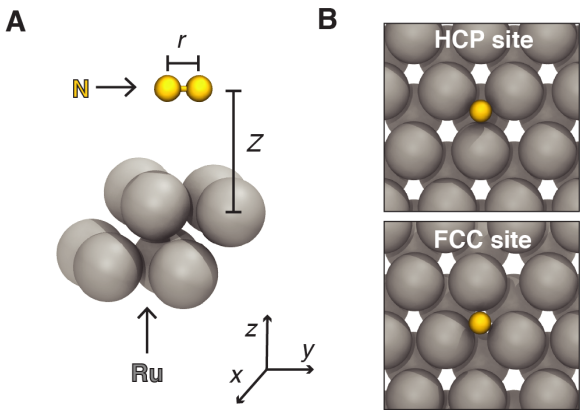

Figure 1. Schematic of the molecular dissociation on Ru(0001). (A) The system is modeled as a nitrogen molecule on a 2x2 unit cell of two-layer Ru(0001) slab with 3D periodic boundary conditions. Two CVs are used to perform enhanced sampling simulations: r (N-N distance) and Z (molecule-surface distance projected along the z-coordinate). (B) There are two stable adsorption sites for nitrogen atoms: HCP and FCC hollow sites. These two sites give rise to an ensemble of possible 2N* states, including HCP-HCP, FCC-FCC, and HCP-FCC configurations.

As demonstrated in Figures 2A-2C, CFF-AIMD successfully samples the configurational space describing the nitrogen dissociation reaction. Using 16 walkers at 1400 K, CFF-AIMD identifies the initial (N_2*) and final states (2N*) of the surface reaction, respectively. By applying the nudged elastic band (NEB) method[52] to the BRANN-fitted FES (Supporting Information), we find the minimum free energy path (MFEP) between the adsorbed molecular state (N_2*) minimum at (r, h) = (1.1, 2.7) Å, where the molecular axis is nearly perpendicular to the surface (the on-top configuration), and the dissociated atomic state (2N*) minimum at (r, h) = (2.7, 1.1) Å, where nitrogen atoms adsorb to predominantly HCP hollow sites. This MFEP has a sharp curvature with a narrow passage through the transition state (TS) (Figure 3C).

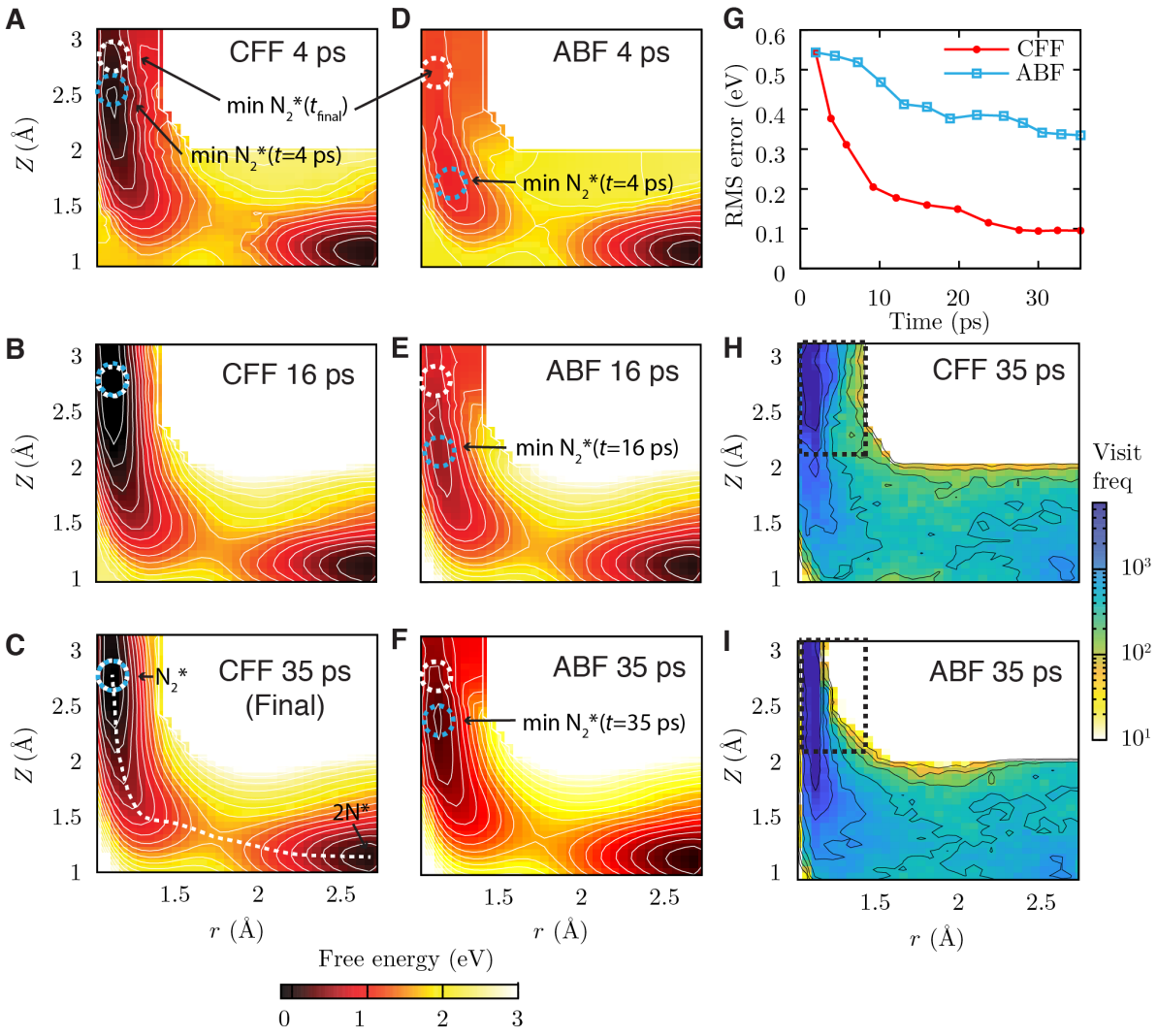

Figure 2. Comparison of two similar enhanced sampling simulation methods with and without neural networks (CFF and ABF). (A-C) 2D FES data from a CFF-AIMD simulation at 1400 K. White and blue circles represent the final converged minima of the N_2* state and the instantaneous free energy minima during the simulation, respectively. CFF correctly identifies the two minima (N_2* and 2N*) within 16 ps of simulation time and is terminated after 35 ps using 16 walkers once the CV space is fully sampled and the root-mean-squared (RMS) error of less than 0.1 eV is reached (see panel **G**). The final FES reveals a dissociation pathway having a narrow transition region and a sharp curve, indicated by the MFEP (white dashed line). (D-F) 2D FES data from a ABF-AIMD simulation at 1400 K. ABF predicts the minimum for the N_2* state incorrectly within the same simulation time as CFF. (G) Changes in the RMS error in free energies, relative to a long independent simulation, over the simulation time (see Supporting Information for the details). CFF converges several times faster than ABF, showing that the use of neural network representation accelerates sampling. (H, I) Biased distributions from CFF and ABF simulations. ABF samples insufficiently samples configurations inside the entrance region (inside the black box), leading to an incorrect N_2* minimum in panel **F**. In contrast, CFF samples configurations more uniformly inside the entrance region that ABF underperforms.

To demonstrate how neural networks accelerate free energy calculations for surface reactions, we perform another set of enhanced sampling simulations using ABF. ABF is chosen as a reference due to the local nature of the mean force at a given point. The potential of mean force is a global property related to the probability distribution of configurations, but the mean force at a given point is independent of other regions within the CV space. For this reason, ABF can refine the estimate locally even when the diffusion through the phase space is slow, making it advantageous for AIMD, as seen in recent studies.[53,54] As illustrated in Figure 2G, CFF converges faster than ABF, reaching an error of ~0.1 eV in the last timestep. Initially, ABF maps out the general FES topology of two minima and a saddle point (Figures 2D-2F). Surprisingly, ABF simulation does not finish sampling the CV space even after a more extended simulation period (~102 ps) (Figure S6C).

The main difference between the two methods lies near the N_2* region in the FES outlined in Figures 2H and 2I. This region, conventionally known as the "entrance channel," is particularly narrow, such that even a small perturbation in r (from 1.1 to 1.5 Å) results in a large change in free energy (~2 eV). The configurational space at the entrance channel from the CFF simulation is sampled more uniformly, relative to the ABF simulation. This sampling discrepancy arises due to how the bias is defined in each method. In ABF, biasing forces are calculated only in visited regions and are set to zero in unvisited regions. Thus, there is a strong discontinuity in the force and free energy estimates between the visited and unvisited region near the entrance channel. On the other hand, neural networks in CFF provide a smooth and continuous representation of the bias. This bias is interpolated over the entire CV space, including regions where data used to train the neural networks (local mean forces and the histogram of the visited configurations) are absent. Accordingly, the neural network-representation of the bias helps the system escape from the

narrow valley defined by the N_2* minimum. These findings highlight the potential of this method for sampling free energy landscapes containing narrow valleys and sharp curvatures, which are common in molecular dissociation on surfaces.

In order to understand the dissociation reaction mechanism, we analyze the trajectories from CFF-AIMD simulations. Snapshots of the surface dissociation reaction process are shown in Figure 3A, and the full process is shown in Movie S1. Initially, the molecular nitrogen adsorbs to the metal with its molecular axis nearly perpendicular to the surface, with an average tilt angle of ϕ=16° (state N_2*), as seen in the angular distribution, $P(\phi)$, plotted in Figure 3B. Thermal rotation causes this on-top configuration to bend toward the surface (state A) and lie flat as ϕ=90° (state M). As the N-N bond stretches, the adsorbate reaches a transition state, where, on average, one nitrogen atom is near an HCP hollow site, while the other approaches the closest FCC hollow site. The other nitrogen atom diffuses to an empty hollow site and the N-N bond breaks. At 700 K, nearly all dissociated nitrogen atoms adsorb to HCP hollow sites (HCP-HCP), the lowest-energy 2N* state predicted from DFT calculations. However, as temperature increases to 1400 K, the nitrogen complex at the transition state dissociate into other 2N* states as well, such as HCP-FCC and FCC-FCC configurations. The fraction of HCP-FCC and FCC-FCC configurations that overlap with the 2N* state minimum increases with increasing temperature, based on calculations using a Delaunay triangulation-based adsorption site analysis[55,56] (Figure S9). These results suggest that there are multiple reaction pathways for N_2 dissociation on Ru(0001) at high temperatures.

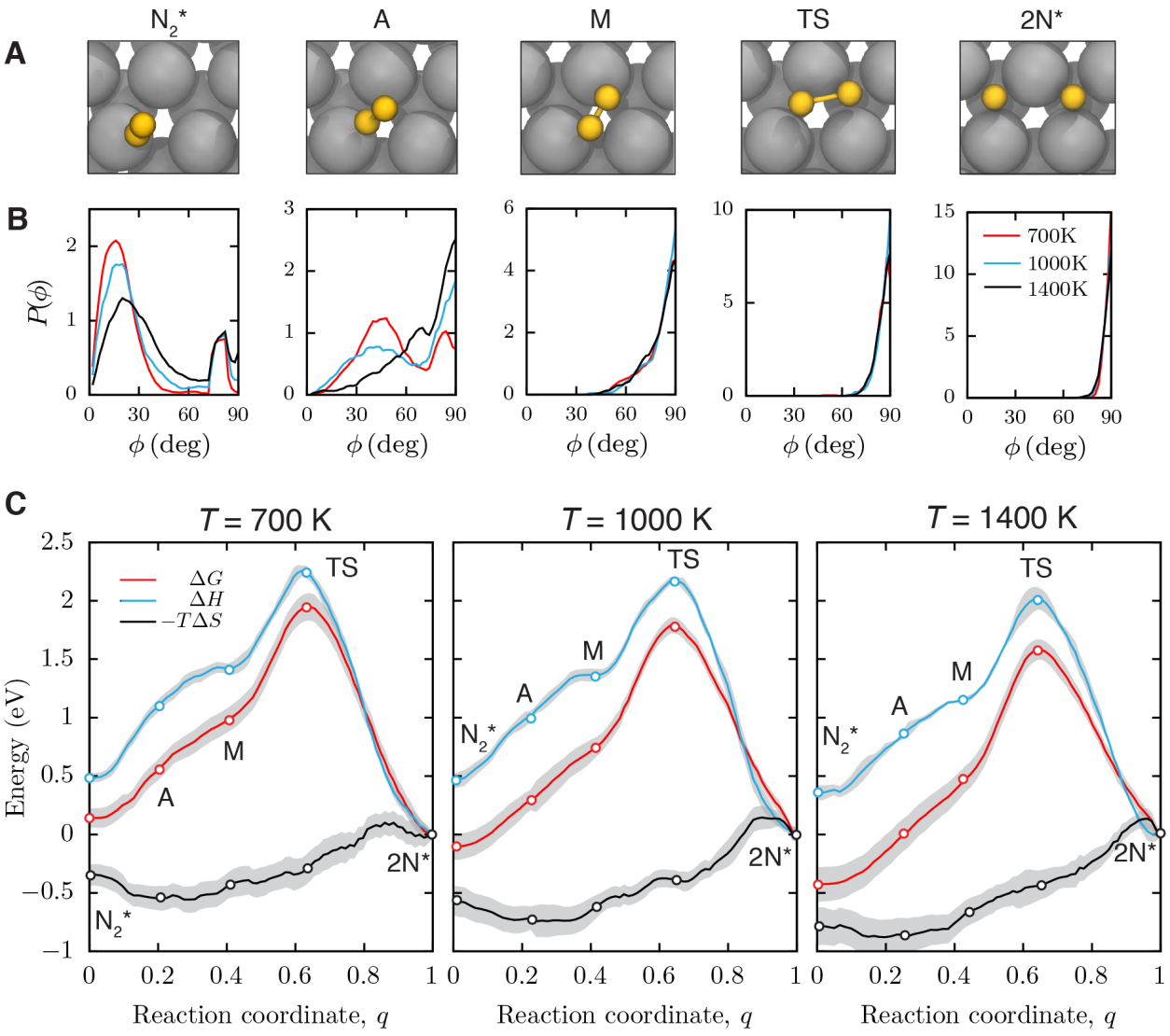

Figure 3. The free energy landscape for the dissociation reaction and its dependence on temperature. (A) A series of snapshots from part of a CFF-AIMD trajectory at 700 K showing changes in the adsorbate configuration as the nitrogen molecule dissociates on Ru(0001): the on-top molecular state (N_2*), tilted adsorbed state (A), flat-lying molecular state (M), transition state (TS), and dissociated state (2N*) at the free energy minimum. (B) Probability distributions of the title angle between the N-N bond and the surface normal (see details of the calculation in the Supporting Information). Molecularly adsorbed states rotate about the molecular axis at high temperatures. (C) 1D free energy, enthalpic, and entropic profiles, referenced to the 2N* state. Entropies of adsorbates states are non-uniform along the reaction coordinate. Reaction free energies (at q=N_2*) and surface reaction barriers (at q=TS) change with the reaction temperature. The local minimum in $\Delta H(q)$ corresponding to state M is absent in $\Delta G(q)$.

To compute the barrier for dissociative adsorption, *i.e.*, $\Delta G = G(\mathrm{TS}) - G(\mathrm{N_{2\,gas}})$,[14,23] we reference relative free energies of adsorbed states from CFF-AIMD to the gas phase, assuming ideal gas behavior for the reference state and HA for the 2N* state (see Supporting Information). Increasing the reaction temperature appreciably raises the dissociation adsorption free energy barrier from 2.02 ± 0.12 eV at 700 K to 2.75 ± 0.09 eV at 1400 K, mainly because the gas phase has higher entropy than the adsorbed state. Laser-assisted associative desorption experiments have reported a barrier of ~2.1 eV with 48 % nitrogen coverage.[14] A recent quasi-classical simulation study based on DFT has determined that a barrier of 1.8 eV with 22 % nitrogen coverage yields agreement with scattering experiments.[18] Notably, our results are predictions for a surface with 50 % nitrogen coverage. Calculated barriers using CFF-AIMD at 700 K are in reasonable agreement with available experimental data within a few tenths of eV. Uncertainty arises because the barrier is known to depend on the exchange-correlational functional in DFT[57] and on the surface converge of nitrogen atoms.[14]

In designing catalysts and reaction processes using microkinetic models, energetics of intermediates and transition states are used to predict chemical kinetics[58]. The computed 1D- and 2D-PMFs for the surface dissociation reaction and the enthalpic and entropic contributions are shown in Figures 3C and 4. The surface reaction free energy, $\Delta G_r = G(\mathrm{2N^*}) - G(\mathrm{N_2^*})$, increases from -0.14 eV to 0.43 eV as temperature increases from 700 K to 1400 K. At low temperature, the surface dissociation reaction favors the product (2N*) while at high temperature, the equilibrium is shifted towards the reactant (N_2*). The predicted activation energy for associative desorption, $\Delta G^{\ddagger} = G(\mathrm{TS}) - G(\mathrm{2N^*})$, decreases from 1.94 eV at 700 K to 1.66 eV at 1400 K. The transition state has higher entropy than the 2N* state ($\Delta S^{\ddagger} > 0$), while the activation enthalpy ($\Delta H^{\ddagger}$) decreases with temperature due to the greater population of higher-enthalpy dissociated states with

increasing temperature. Therefore, the combined effect from enthalpic and entropic contributions causes $\Delta G^{\ddagger}$ to decrease at higher temperature.

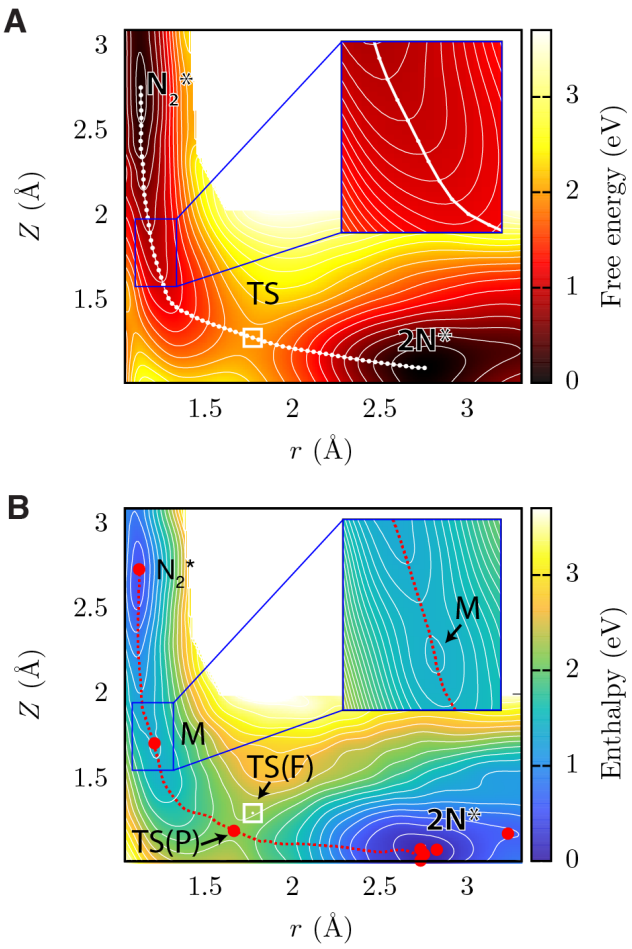

Figure 4. Intermediate states and minimum energy paths of the potential and free energy surfaces. (A) 2D PMF, $\Delta G(r, Z)$, relative to the 2N* state, computed from CFF-AIMD simulations at 700 K. Only three critical points (N_2*, TS, and 2N* states in white square markers) are identified along the MFEP (white line). (B) Average potential energy or enthalpic contribution to the free energy, $\Delta H(r, Z)$, of the same system as in panel (A). Critical points on the PES found from energy minimization and transition state search methods (in red circles) coincide well with the topology of $\Delta H(r, Z)$, The minimum potential energy path computed from $\Delta H(r, Z)$ indicates that the TS on the PES (in red circle) lies closer to the surface than the TS on the FES (in white square marker). Inset figures are zoomed views near state M predicted from energy minimization. While a local minimum corresponding to state M is found in $\Delta H(r, Z)$, it is absent in $\Delta G(r, Z)$. The energy difference between successive contour lines is 0.2 eV in main figures and 0.05 eV in inset figures.

In addition to the energetics, we find differences in the critical points between FES and PES. Critical points on the PES were identified using energy minimization and transition state search methods (see the Computational Methods). A shallow local energy minimum corresponding to state M, also predicted from energy minimization, is seen ~1 eV above the N_2* state in averaged potential energy (or enthalpic) profiles computed from CFF-AIMD (Figures 3C and 4B). This intermediate state has been described in previous works as an additional metastable molecularly adsorbed state.[10,17] Interestingly, this minimum is absent in 1D- and 2D-PMFs (Figures 3C and 4A). Thus, state M is not a true metastable state within our model at the temperatures studied. We also find that entropy causes a shift in the MFEP (Figure 4A) relative to the minimum potential energy path (Figure 4B). Consequently, the transition state found from PES (see Computational Methods) lies closer to the Ru surface than the prediction from CFF-AIMD by 0.1 Å. Methods using critical points of the PES to predict free energy diagrams assume that entropy plays a minor role in determining intermediate and transition states. Our findings suggest the merit of directly identifying critical points from the FES, especially for systems with significant entropic effects.

To understand the origins of temperature-dependent contributions to the energetics of the reaction process, we compare findings from CFF-AIMD simulations to those from HA (Figure 5), which uses critical points of the PES and captures the vibrational entropy and enthalpy based on normal-mode analysis, zero-point vibrational energy (ZPE) effects, and configurational entropy (see Computational Methods). As seen in Table S1, there is a good agreement in HA results using quantum and classical harmonic approximation for this reaction at the temperatures studied in this work, providing evidence that quantum effects such as ZPE do not substantially affect the comparisons made in this work.

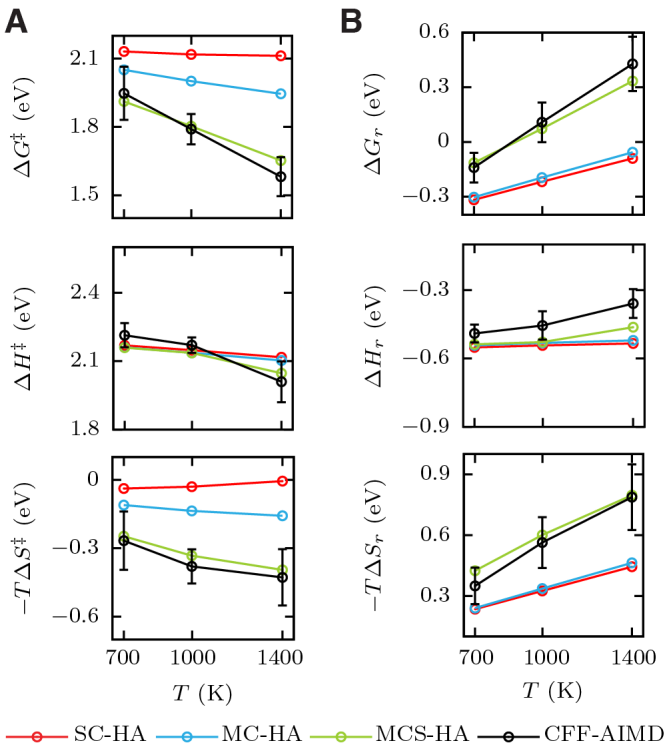

Figure 5. Comparison of thermodynamic quantities computed using CFF-AIMD and several different HA methods (SC-, MC-, and MCS-HA). (A) Effect of temperature on the free energy (top), enthalpy (middle), and entropy (bottom) of the associative desorption of N_2, $\Delta E^{\ddagger} = E(\mathrm{TS}) - E(2\mathrm{N}^*)$. (B) Same as panel (A) but on the surface reaction energy, $\Delta E_r = E(2\mathrm{N}^*) - E(\mathrm{N_2}^*)$. The largest deviations between the two methods are seen using SC-HA. There is a good agreement between MCS-HA and CFF-AIMD, showing that additional temperature-dependent effects captured by CFF-AIMD can be explained by configurational degeneracy, thermal averaging of multiple adsorbed states, and vibrational entropy of surface atoms.

Similar to previous DFT studies of molecular dissociation on metal surfaces,[6] we first consider HA calculations using the single lowest-energy configuration for each state (N_2*, TS, and 2N*) and only the normal modes of the adsorbate (N atoms) without the surface atoms. This is the most conventional usage of HA in the context of surface science, and we term this approach "single configuration HA" (SC-HA). As shown in Figure 5, there are large deviations in free energies between SC-HA and CFF-AIMD in the associative desorption barrier and the surface reaction energy, which are also statistically significant. Surprisingly, the two methods predict opposite

trends for the temperature-dependence of $\Delta S^{\ddagger}(T)$. The $T\Delta S^{\ddagger}(T)$ term is nearly zero and shows a decreasing trend with temperature in SC-HA, while it is much greater than zero and increases with increasing temperature in CFF-AIMD.

There are several possible sources of entropic effects beyond SC-HA in CFF-AIMD, including the anharmonicity, configurational entropy of adsorbates, and vibrational entropy due to mobile surface atoms. The analysis on vibrational anharmonicity demonstrates that 2N*, N_2*, and TS states are mostly harmonic (Figure S5), though there can be other types of anharmonicity, such as the rotational entropy. Based on multiple 2N* states observed in CFF-AIMD simulations, we consider an ensemble of adsorbate configurations in HA, which we refer to as "multiple configuration HA" (MC-HA), (see Supporting Information). As illustrated in Figure 3, CFF-AIMD demonstrates better agreement in $\Delta G^{\ddagger}(T)$ with MC-HA than with SC-HA, especially in the temperature-dependence of $\Delta S^{\ddagger}(T)$. However, there is a minor change in $\Delta S_r(T)$ between MC-HA and SC-HA because configurational entropies of N_2* and 2N* states are comparable. To understand the remaining discrepancy between HA and CFF-AIMD, we also include the vibrational entropy from the mobile surface atoms, called "multiple configurations with surface atoms" (MCS-HA). Comparing MCS-HA and CFF-AIMD results, we find a good agreement between the two methods even at higher temperatures. This finding shows that the change in vibrational entropy of the surface atoms in elementary reactions can be substantial, although this effect is often neglected in studies of reactions on transition metal surfaces.

We computed the free energy landscape of a prototypical metal catalyzed reaction, the dissociation of N_2 on Ru(0001), using a neural network-based enhanced sampling method, CFF-AIMD. We find that the PMF for the adsorbed N_2 dissociating on the metal contains two deep minima with a narrow transition pathway, and that the energetic barriers are consistent with

experiments. Our neural network-based method adaptively refines under-visited regions of the FES by estimating the mean forces and frequencies of visits, thus accelerating enhanced sampling simulations. The predicted enthalpic energy surface shows a previously reported molecularly adsorbed intermediate state that is absent in the FES, which may not be predicted using harmonic PES-based methods alone. Results from several variants of HA show that there are significant differences in temperature-dependent thermodynamic quantities between CFF-AIMD and the standard harmonic approximation because of the configurational entropy, thermal averaging of multiple states, the surface atom vibrational modes, and possible anharmonic contributions, all of which are captured automatically by the CFF-AIMD method. These findings suggest that the free energy of the adsorbed states can depend on the entropic contributions of both the adsorbate and the metal surface atoms, even for the case of a diatomic species dissociating on a solid transition metal catalyst.

Generalizable, efficient free energy methods are key for studying surface reactions that exhibit appreciable entropic effects to reaction energies, such as those involving large adsorbates, solvent-electrolyte species, and soft or porous surfaces such as MOFs. Machine learning-assisted enhanced sampling approaches, such as CFF-AIMD, can discover and elucidate the reaction mechanisms for these complex systems.

COMPUTATIONAL METHODS

System Setup. DFT was used to model N_2 dissociation reaction on Ru(0001). DFT calculations were carried out using the Perdew-Burke-Ernzerhof (PBE) exchange-correlational functional[59] as implemented in the Qbox code.[60,61] The system was modeled as a nitrogen molecule on a 2x2 unit cell of two-layer Ru(0001) slab with periodic boundary condition in 3D (Figure 1A). A vacuum

spacing of 10 Å in the direction normal to the surface plane was included to avoid interaction across periodic images. The ion cores were described using Optimized Norm-Conserving Vanderbilt pseudopotentials from the SG15 library[62,63], and a plane-wave basis for the valence electrons was used with an energy cutoff of 50 Ry, $2 \times 2 \times 1$ k-point mesh, and Fermi smearing with electronic temperature of 1090 K. PBE tends to over-bind adsorbates to surfaces by a few tenths of eV[57], and combined with our DFT benchmark studies (Supporting Information), an overall DFT error in predicted barriers can be on the order of tenths of eV.

Enhanced Sampling Simulations. CFF-AIMD[47] and ABF-AIMD[64] were used to compute the PMF or the FES for the dissociation reaction using the SSAGES software package[65] coupled to the AIMD software Qbox. AIMD and enhanced sampling simulations were performed at the NVT ensemble using the Bussi-Donadio-Parrinello thermostat[67] with a time step of 0.483 fs at each temperature setting (700 K, 1000 K, and 1400 K). Adsorbate complexes with varying N-N bond lengths were equilibrated at finite temperature using 5 ps-long AIMD simulations. Two CVs (r, Z) were chosen to compute free energies (Figure 1A). A 2D non-rectangular CV grid is used to avoid unphysical, high energy regions (> 4 eV) (Figure S6). The FES was evaluated by integrating mean forces over the CV grid to directly compare CFF and ABF. To provide statistical uncertainties of the PMF, we averaged over three independent enhanced sampling simulations and calculated the standard deviation. Descriptions of CFF-AIMD simulations are in the Supporting Information.

Harmonic Approximation. In free energy calculations using HA, initial and final states of the reaction were determined using energy minimization, and transition states were identified via the fixed bond length method,[68] which was benchmarked against the climbing image nudge elastic band method.[69] The thermochemistry module in the Atomic Simulation Environment (ASE)[70] was

used to perform temperature-dependent corrections to energies of adsorbed states (HA) and the gas phase (ideal gas approximation at pressure of 150 bar). Supporting Information includes descriptions of HA and transition state search calculations.

ACKNOWLEDGMENT

We thank Alan C. Luntz for helpful discussions. E.M.Y.L. thanks Alvin Yu for a careful reading of the manuscript and providing scientific commentary. This work is supported by the Midwest Integrated Center for Computational Materials (MICCoM) as part of the Computational Materials Sciences Program funded by the U.S. Department of Energy, Office of Science, Basic Energy Sciences, Materials Sciences and Engineering Division, through Argonne National Laboratory, under Contract No. DE-AC02-06CH11357. T.L., A.R.S., and J.K.N. acknowledge support from the SUNCAT Center for Interface Science and Catalysis as part of the U.S. Department of Energy, Office of Science, Office of Basic Energy Sciences, Chemical Sciences, Geosciences, and Biosciences Division, Catalysis Science Program; and Villum Fonden, part of the Villum Center for the Science of Sustainable Fuels and Chemicals (V-SUSTAIN grant 9455). T.L. acknowledges support from the US Department of Energy through the Computational Sciences Graduate Fellowship (DOE CSGF) under grant number DE-FG02-97ER25308. This research used computing resources provided by Bebop, a high-performance computing cluster operated by the Laboratory Computing Resource Center (LCRC) at Argonne National Laboratory, the University of Chicago Research Computing Center (RCC), Stanford Research Computing Center (SRCC), and the National Energy Research Scientific Computing Center (NERSC) supported by the Office of Science of the U.S. Department of Energy under Contract No. DE-AC02-05CH11231.

REFERENCES

(1) Nørskov, J. K.; Abild-Pedersen, F.; Studt, F.; Bligaard, T. Density Functional Theory in Surface Chemistry and Catalysis. *Proc Natl Acad Sci USA* **2011**, *108* (3), 937–943. https://doi.org/10.1073/pnas.1006652108.

(2) Nørskov, J. K.; Studt, F.; Abild-Pedersen, F.; Bligaard, T. Fundamental Concepts in Heterogeneous Catalysis; 2014. https://doi.org/10.1002/9781118892114.

(3) Lansford, J. L.; Vlachos, D. G. Infrared Spectroscopy Data- and Physics-Driven Machine Learning for Characterizing Surface Microstructure of Complex Materials. *Nat Commun* **2020**, *11* (1), 1513. https://doi.org/10.1038/s41467-020-15340-7.

(4) Pattabathula, V.; Richardson, J. Introduction to Ammonia Production. *CEP Magazine*. 2016, pp 69–75.

(5) Liu, H. Ammonia Synthesis Catalyst 100 Years: Practice, Enlightenment and Challenge. *Chinese J. Catalysis* **2014**, *35* (10), 1619–1640. https://doi.org/10.1016/S1872-2067(14)60118-2.

(6) Honkala, K.; Hellman, A.; Remediakis, I. N.; Logadottir, A.; Carlsson, A.; Dahl, S.; Christensen, C. H.; Nørskov, J. K. Ammonia Synthesis from First-Principles Calculations. *Science* **2005**, *307* (5709), 555–558. https://doi.org/10.1126/science.1106435.

(7) Tsai, W.; Weinberg, W. H. Steady-State Decomposition of Ammonia on the Ruthenium(001) Surface. *J. Phys. Chem.* **1987**, *91* (20), 5302–5307. https://doi.org/10.1021/j100304a034.

(8) Shi, H.; Jacobi, K.; Ertl, G. Dissociative Chemisorption of Nitrogen on Ru(0001). *J. Chem. Phys.* **1993**, *99* (11), 9248–9254. https://doi.org/10.1063/1.465541.

(9) Romm, L.; Katz, G.; Kosloff, R.; Asscher, M. Dissociative Chemisorption of N2 on Ru(001) Enhanced by Vibrational and Kinetic Energy: Molecular Beam Experiments and Quantum Mechanical Calculations. *J. Phys. Chem. B* **1997**, *101* (12), 2213–2217. https://doi.org/10.1021/jp962599o.

(10) Murphy, M. J.; Skelly, J. F.; Hodgson, A.; Hammer, B. Inverted Vibrational Distributions from N2 Recombination at Ru(001): Evidence for a Metastable Molecular Chemisorption Well. *J. Chem. Phys.* **1999**, *110* (14), 6954–6962. https://doi.org/10.1063/1.478601.

(11) Diekhöner, L.; Mortensen, H.; Baurichter, A.; Luntz, A. C. Coverage Dependence of Activation Barriers: Nitrogen on Ru(0001). *J. Vac. Sci. Technol. A* **2000**, *18* (4), 1509–1513. https://doi.org/10.1116/1.582376.

(12) Diekhöner, L.; Mortensen, H.; Baurichter, A.; Luntz, A. C.; Hammer, B. Dynamics of High-Barrier Surface Reactions: Laser-Assisted Associative Desorption of N2 from Ru(0001). *Phys. Rev. Lett.* **2000**, *84* (21), 4906–4909. https://doi.org/10.1103/PhysRevLett.84.4906.

(13) Romm, L.; Citri, O.; Kosloff, R.; Asscher, M. A Remarkable Heavy Atom Isotope Effect in the Dissociative Chemisorption of Nitrogen on Ru(001). *J. Chem. Phys.* **2000**, *112* (19), 8221–8224. https://doi.org/10.1063/1.481476.

(14) Diekhöner, L.; Mortensen, H.; Baurichter, A.; Luntz, A. C. Laser Assisted Associative Desorption of N2 and CO from Ru(0001). *J. Chem. Phys.* **2001**, *115* (7), 3356–3373. https://doi.org/10.1063/1.1386810.

(15) Dietrich, H.; Geng, P.; Jacobi, K.; Ertl, G. Sticking Coefficient for Dissociative Adsorption of N2 on Ru Single-crystal Surfaces. *J. Chem. Phys.* **1996**, *104* (1), 375–381. https://doi.org/10.1063/1.470836.

(16) Hammer, B.; Nørskov, J. K. Theoretical Surface Science and Catalysis—Calculations and Concepts. In *Advances in Catalysis*; Impact of Surface Science on Catalysis; Academic Press, 2000; Vol. 45, pp 71–129. https://doi.org/10.1016/S0360-0564(02)45013-4.
(17) Mortensen, J. J.; Morikawa, Y.; Hammer, B.; Nørskov, J. K. Density Functional Calculations of N2 Adsorption and Dissociation on a Ru(0001) Surface. *J. Catal.* **1997**, *169* (1), 85–92. https://doi.org/10.1006/jcat.1997.1661.
(18) Shakouri, K.; Behler, J.; Meyer, J.; Kroes, G.-J. Accurate Neural Network Description of Surface Phonons in Reactive Gas–Surface Dynamics: N2 + Ru(0001). *J. Phys. Chem. Lett.* **2017**, *8* (10), 2131–2136. https://doi.org/10.1021/acs.jpclett.7b00784.
(19) Spiering, P.; Shakouri, K.; Behler, J.; Kroes, G.-J.; Meyer, J. Orbital-Dependent Electronic Friction Significantly Affects the Description of Reactive Scattering of N2 from Ru(0001). *J. Phys. Chem. Lett.* **2019**, *10* (11), 2957–2962. https://doi.org/10.1021/acs.jpclett.9b00523.
(20) Díaz, C.; Vincent, J. K.; Krishnamohan, G. P.; Olsen, R. A.; Kroes, G. J.; Honkala, K.; Nørskov, J. K. Multidimensional Effects on Dissociation of N2 on Ru(0001). *Phys. Rev. Lett.* **2006**, *96* (9), 096102. https://doi.org/10.1103/PhysRevLett.96.096102.
(21) Mortensen, J. J.; Hammer, B.; Nørskov, J. K. Alkali Promotion of N2 Dissociation over Ru(0001). *Phys. Rev. Lett.* **1998**, *80* (19), 4333–4336. https://doi.org/10.1103/PhysRevLett.80.4333.
(22) Dahl, S.; Logadottir, A.; Egeberg, R. C.; Larsen, J. H.; Chorkendorff, I.; Törnqvist, E.; Nørskov, J. K. Role of Steps in N2 Activation on Ru(0001). *Phys. Rev. Lett.* **1999**, *83* (9), 1814–1817. https://doi.org/10.1103/PhysRevLett.83.1814.
(23) Mallikarjun Sharada, S.; Bligaard, T.; Luntz, A. C.; Kroes, G.-J.; Nørskov, J. K. SBH10: A Benchmark Database of Barrier Heights on Transition Metal Surfaces. *J. Phys. Chem. C* **2017**, *121* (36), 19807–19815. https://doi.org/10.1021/acs.jpcc.7b05677.
(24) Riss, A.; Paz, A. P.; Wickenburg, S.; Tsai, H.-Z.; De Oteyza, D. G.; Bradley, A. J.; Ugeda, M. M.; Gorman, P.; Jung, H. S.; Crommie, M. F.; Rubio, A.; Fischer, F. R. Imaging Single-Molecule Reaction Intermediates Stabilized by Surface Dissipation and Entropy. *Nat. Chem.* **2016**, *8* (7), 678–683. https://doi.org/10.1038/nchem.2506.
(25) Sauer, J. Ab Initio Calculations for Molecule–Surface Interactions with Chemical Accuracy. *Acc. Chem. Res.* **2019**, *52* (12), 3502–3510. https://doi.org/10.1021/acs.accounts.9b00506.
(26) Sun, J.-J.; Cheng, J. Solid-to-Liquid Phase Transitions of Sub-Nanometer Clusters Enhance Chemical Transformation. *Nat. Commun.* **2019**, *10* (1), 5400. https://doi.org/10.1038/s41467-019-13509-3.
(27) Collinge, G.; Yuk, S. F.; Nguyen, M.-T.; Lee, M.-S.; Glezakou, V.-A.; Rousseau, R. Effect of Collective Dynamics and Anharmonicity on Entropy in Heterogenous Catalysis: Building the Case for Advanced Molecular Simulations. *ACS Catal.* **2020**, 9236–9260. https://doi.org/10.1021/acscatal.0c01501.
(28) Flaherty, D. W.; Iglesia, E. Transition-State Enthalpy and Entropy Effects on Reactivity and Selectivity in Hydrogenolysis of n-Alkanes. *J. Am. Chem. Soc.* **2013**, *135* (49), 18586–18599. https://doi.org/10.1021/ja4093743.
(29) Shakouri, K.; Behler, J.; Meyer, J.; Kroes, G.-J. Analysis of Energy Dissipation Channels in a Benchmark System of Activated Dissociation: N2 on Ru(0001). *J. Phys. Chem. C* **2018**, *122* (41), 23470–23480. https://doi.org/10.1021/acs.jpcc.8b06729.
(30) Jiang, B.; Li, J.; Guo, H. High-Fidelity Potential Energy Surfaces for Gas-Phase and Gas–Surface Scattering Processes from Machine Learning. *J. Phys. Chem. Lett.* **2020**. https://doi.org/10.1021/acs.jpclett.0c00989.

(31) Senftle, T. P.; Hong, S.; Islam, M. M.; Kylasa, S. B.; Zheng, Y.; Shin, Y. K.; Junkermeier, C.; Engel-Herbert, R.; Janik, M. J.; Aktulga, H. M.; Verstraelen, T.; Grama, A.; van Duin, A. C. T. The ReaxFF Reactive Force-Field: Development, Applications and Future Directions. *npj Comput Mater* **2016**, *2* (1), 15011. https://doi.org/10.1038/npjcompumats.2015.11.

(32) Goikoetxea, I.; Alducin, M.; Díez Muiño, R.; Juaristi, J. I. Dissociative and Non-Dissociative Adsorption Dynamics of N2 on Fe(110). *Phys. Chem. Chem. Phys.* **2012**, *14* (20), 7471. https://doi.org/10.1039/c2cp40229g.

(33) Sun, G.; Jiang, H. Ab Initio Molecular Dynamics with Enhanced Sampling for Surface Reaction Kinetics at Finite Temperatures: CH2 ⇌ CH + H on Ni(111) as a Case Study. *J. Chem. Phys.* **2015**, *143* (23), 234706. https://doi.org/10.1063/1.4937483.

(34) Herron, J. A.; Morikawa, Y.; Mavrikakis, M. Ab Initio Molecular Dynamics of Solvation Effects on Reactivity at Electrified Interfaces. *Proc Natl Acad Sci USA* **2016**, *113* (34), E4937–E4945. https://doi.org/10.1073/pnas.1604590113.

(35) Cheng, T.; Xiao, H.; Goddard, W. A. Full Atomistic Reaction Mechanism with Kinetics for CO Reduction on Cu(100) from Ab Initio Molecular Dynamics Free-Energy Calculations at 298 K. *Proc Natl Acad Sci USA* **2017**, *114* (8), 1795–1800. https://doi.org/10.1073/pnas.1612106114.

(36) Kristoffersen, H. H.; Chan, K.; Vegge, T.; Hansen, H. A. Energy–Entropy Competition in Cation–Hydroxyl Interactions at the Liquid Water–Pt(111) Interface. *Chem. Commun.* **2020**, *56* (3), 427–430. https://doi.org/10.1039/C9CC07769C.

(37) Martínez-Suárez, L.; Siemer, N.; Frenzel, J.; Marx, D. Reaction Network of Methanol Synthesis over Cu/ZnO Nanocatalysts. *ACS Catal.* **2015**, *5* (7), 4201–4218. https://doi.org/10.1021/acscatal.5b00442.

(38) Réocreux, R.; Michel, C.; Fleurat-Lessard, P.; Sautet, P.; Steinmann, S. N. Evaluating Thermal Corrections for Adsorption Processes at the Metal/Gas Interface. *J. Phys. Chem. C* **2019**, *123* (47), 28828–28835. https://doi.org/10.1021/acs.jpcc.9b09863.

(39) Guo, C.; Wang, Z.; Wang, D.; Wang, H.-F.; Hu, P. First-Principles Determination of CO Adsorption and Desorption on Pt(111) in the Free Energy Landscape. *J. Phys. Chem. C* **2018**, *122* (37), 21478–21483. https://doi.org/10.1021/acs.jpcc.8b06782.

(40) Réocreux, R.; Girel, É.; Clabaut, P.; Tuel, A.; Besson, M.; Chaumonnot, A.; Cabiac, A.; Sautet, P.; Michel, C. Reactivity of Shape-Controlled Crystals and Metadynamics Simulations Locate the Weak Spots of Alumina in Water. *Nature Communications* **2019**, *10* (1), 3139. https://doi.org/10.1038/s41467-019-10981-9.

(41) Foppa, L.; Iannuzzi, M.; Copéret, C.; Comas-Vives, A. Adlayer Dynamics Drives CO Activation in Ru-Catalyzed Fischer–Tropsch Synthesis. *ACS Catal.* **2018**, *8* (8), 6983–6992. https://doi.org/10.1021/acscatal.8b01232.

(42) Ludwig, T.; Singh, A. R.; Nørskov, J. K. Subsurface Nitrogen Dissociation Kinetics in Lithium Metal from Metadynamics. *J. Phys. Chem. C* **2020**, 11.

(43) Bernardi, R. C.; Melo, M. C. R.; Schulten, K. Enhanced Sampling Techniques in Molecular Dynamics Simulations of Biological Systems. *Biochimica et Biophysica Acta (BBA) - General Subjects* **2015**, *1850* (5), 872–877. https://doi.org/10.1016/j.bbagen.2014.10.019.

(44) Yu, A.; Lee, E. M. Y.; Jin, J.; Voth, G. A. Atomic-Scale Characterization of Mature HIV-1 Capsid Stabilization by Inositol Hexakisphosphate (IP6). *Sci. Adv.* **2020**, *6*, eabc6465. https://doi.org/10.1126/sciadv.abc6465.

(45) Yu, A.; Lau, A. Y. Energetics of Glutamate Binding to an Ionotropic Glutamate Receptor. *J. Phys. Chem. B* **2017**, *121* (46), 10436–10442. https://doi.org/10.1021/acs.jpcb.7b06862.
(46) Guo, A. Z.; Sevgen, E.; Sidky, H.; Whitmer, J. K.; Hubbell, J. A.; de Pablo, J. J. Adaptive Enhanced Sampling by Force-Biasing Using Neural Networks. *J. Chem. Phys.* **2018**, *148* (13), 134108. https://doi.org/10.1063/1.5020733.
(47) Sevgen, E.; Guo, A. Z.; Sidky, H.; Whitmer, J. K.; de Pablo, J. J. Combined Force-Frequency Sampling for Simulation of Systems Having Rugged Free Energy Landscapes. *J. Chem. Theory Comput.* **2020**, *16* (3), 1448–1455. https://doi.org/10.1021/acs.jctc.9b00883.
(48) Sidky, H.; Whitmer, J. K. Learning Free Energy Landscapes Using Artificial Neural Networks. *J. Chem. Phys.* **2018**, *148* (10), 104111. https://doi.org/10.1063/1.5018708.
(49) Zhang, J.; Yang, Y. I.; Noé, F. Targeted Adversarial Learning Optimized Sampling. *J. Phys. Chem. Lett.* **2019**, *10* (19), 5791–5797. https://doi.org/10.1021/acs.jpclett.9b02173.
(50) Bonati, L.; Zhang, Y.-Y.; Parrinello, M. Neural Networks-Based Variationally Enhanced Sampling. *Proc Natl Acad Sci USA* **2019**, *116* (36), 17641–17647. https://doi.org/10.1073/pnas.1907975116.
(51) Zhang, L.; Wang, H.; E, W. Reinforced Dynamics for Enhanced Sampling in Large Atomic and Molecular Systems. *The Journal of Chemical Physics* **2018**, *148* (12), 124113. https://doi.org/10.1063/1.5019675.
(52) Henkelman, G.; Jónsson, H. Improved Tangent Estimate in the Nudged Elastic Band Method for Finding Minimum Energy Paths and Saddle Points. *J. Chem. Phys.* **2000**, *113* (22), 9978–9985. https://doi.org/10.1063/1.1323224.
(53) Sevgen, E.; Giberti, F.; Sidky, H.; Whitmer, J. K.; Galli, G.; Gygi, F.; de Pablo, J. J. Hierarchical Coupling of First-Principles Molecular Dynamics with Advanced Sampling Methods. *J. Chem. Theory Comput.* **2018**, *14* (6), 2881–2888. https://doi.org/10.1021/acs.jctc.8b00192.
(54) Zhang, C.; Giberti, F.; Sevgen, E.; de Pablo, J. J.; Gygi, F.; Galli, G. Dissociation of Salts in Water under Pressure. *Nat Commun* **2020**, *11* (1), 3037. https://doi.org/10.1038/s41467-020-16704-9.
(55) Ong, S. P.; Richards, W. D.; Jain, A.; Hautier, G.; Kocher, M.; Cholia, S.; Gunter, D.; Chevrier, V. L.; Persson, K. A.; Ceder, G. Python Materials Genomics (Pymatgen): A Robust, Open-Source Python Library for Materials Analysis. *Comput. Mater. Sci.* **2013**, *68*, 314–319. https://doi.org/10.1016/j.commatsci.2012.10.028.
(56) Montoya, J. H.; Persson, K. A. A High-Throughput Framework for Determining Adsorption Energies on Solid Surfaces. *npj Comput. Mater.* **2017**, *3* (1), 1–4. https://doi.org/10.1038/s41524-017-0017-z.
(57) Wellendorff, J.; Lundgaard, K. T.; Møgelhøj, A.; Petzold, V.; Landis, D. D.; Nørskov, J. K.; Bligaard, T.; Jacobsen, K. W. Density Functionals for Surface Science: Exchange-Correlation Model Development with Bayesian Error Estimation. *Phys. Rev. B* **2012**, *85* (23), 235149. https://doi.org/10.1103/PhysRevB.85.235149.
(58) Dumesic, J. A.; Rudd, D. F.; Aparicio, L. M.; Rekoske, J. E.; Treviño, A. A. *The Microkinetics of Heterogeneous Catalysis*, 1st Edition.; American Chemical Society: Washington, DC, 1993.
(59) Perdew, J. P.; Burke, K.; Ernzerhof, M. Generalized Gradient Approximation Made Simple. *Phys. Rev. Lett.* **1996**, *77* (18), 3865–3868. https://doi.org/10.1103/PhysRevLett.77.3865.

(60) Gygi, F. Architecture of Qbox: A Scalable First-Principles Molecular Dynamics Code. *IBM J. Res. Dev.* **2008**, *52* (1.2), 137–144. https://doi.org/10.1147/rd.521.0137.
(61) Qbox First-Principles Molecular Dynamics Code http://qboxcode.org (accessed Jul 13, 2019).
(62) Schlipf, M.; Gygi, F. Optimization Algorithm for the Generation of ONCV Pseudopotentials. *Comput. Phys. Commun.* **2015**, *196*, 36–44. https://doi.org/10.1016/j.cpc.2015.05.011.
(63) Hamann, D. R. Optimized Norm-Conserving Vanderbilt Pseudopotentials. *Phys. Rev. B* **2013**, *88* (8), 085117. https://doi.org/10.1103/PhysRevB.88.085117.
(64) Darve, E.; Rodríguez-Gómez, D.; Pohorille, A. Adaptive Biasing Force Method for Scalar and Vector Free Energy Calculations. *J. Chem. Phys.* **2008**, *128* (14), 144120. https://doi.org/10.1063/1.2829861.
(65) Sidky, H.; Colón, Y. J.; Helfferich, J.; Sikora, B. J.; Bezik, C.; Chu, W.; Giberti, F.; Guo, A. Z.; Jiang, X.; Lequieu, J.; Li, J.; Moller, J.; Quevillon, M. J.; Rahimi, M.; Ramezani-Dakhel, H.; Rathee, V. S.; Reid, D. R.; Sevgen, E.; Thapar, V.; Webb, M. A.; Whitmer, J. K.; de Pablo, J. J. SSAGES: Software Suite for Advanced General Ensemble Simulations. *J. Chem. Phys.* **2018**, *148* (4), 044104. https://doi.org/10.1063/1.5008853.
(66) SSAGES: Software Suite for Advanced General Ensemble Simulations https://ssagesproject.github.io/ (accessed Jun 15, 2020).
(67) Bussi, G.; Donadio, D.; Parrinello, M. Canonical Sampling through Velocity Rescaling. *J. Chem. Phys.* **2007**, *126* (1), 014101. https://doi.org/10.1063/1.2408420.
(68) Alavi, A.; Hu, P.; Deutsch, T.; Silvestrelli, P. L.; Hutter, J. CO Oxidation on Pt(111): An *Ab Initio* Density Functional Theory Study. *Phys. Rev. Lett.* **1998**, *80* (16), 3650–3653. https://doi.org/10.1103/PhysRevLett.80.3650.
(69) Henkelman, G.; Uberuaga, B. P.; Jónsson, H. A Climbing Image Nudged Elastic Band Method for Finding Saddle Points and Minimum Energy Paths. *The Journal of Chemical Physics* **2000**, *113* (22), 9901–9904. https://doi.org/10.1063/1.1329672.
(70) Hjorth Larsen, A.; Jørgen Mortensen, J.; Blomqvist, J.; Castelli, I. E.; Christensen, R.; Dułak, M.; Friis, J.; Groves, M. N.; Hammer, B.; Hargus, C.; Hermes, E. D.; Jennings, P. C.; Bjerre Jensen, P.; Kermode, J.; Kitchin, J. R.; Leonhard Kolsbjerg, E.; Kubal, J.; Kaasbjerg, K.; Lysgaard, S.; Bergmann Maronsson, J.; Maxson, T.; Olsen, T.; Pastewka, L.; Peterson, A.; Rostgaard, C.; Schiøtz, J.; Schütt, O.; Strange, M.; Thygesen, K. S.; Vegge, T.; Vilhelmsen, L.; Walter, M.; Zeng, Z.; Jacobsen, K. W. The Atomic Simulation Environment-a Python Library for Working with Atoms. *J Phys Condens Matter* **2017**, *29* (27), 273002. https://doi.org/10.1088/1361-648X/aa680e.